Microcarriers promote the through interface movement of mouse trophoblast stem cells by regulating stiffness

Zili Gao [a,b,c,1], Jia Guo [a,b,c,1], Bo Gou [a,b,c,1], Zhen Gu [d], Tan Jia [a,b,c], Sinan Ma [a,b,e], Liyuan Jiang [a,b,e], Wenli Liu [a,b], Lixun Zhou [a,b], Qi Gu [a,b,c,*]

[a] State Key Laboratory of Membrane Biology, The State Key Laboratory of Stem Cell and Reproductive Biology, Institute of Zoology, Chinese Academy of Sciences, Beijing, 100101, PR China
[b] Beijing Institute for Stem Cell and Regenerative Medicine, Beijing, 100101, PR China
[c] University of Chinese Academy of Sciences, Beijing, 100049, PR China
[d] Department of Chemistry and Biological Engineering, University of Science and Technology, Beijing, 100083, PR China
[e] School of Life Sciences, Northeast Agricultural University, Harbin, 150030, PR China

ARTICLE INFO

ABSTRACT

Mechanical force is crucial in the whole process of embryonic development. However, the role of trophoblast mechanics during embryo implantation has rarely been studied. In this study, we constructed a model to explore the effect of stiffness changes in mouse trophoblast stem cells (mTSCs) on implantation: microcarrier was prepared by sodium alginate using a droplet microfluidics system, and mTSCs were attached to the microcarrier surface with laminin modifications, called T(micro). Compared with the spheroid, formed by the self-assembly of mTSCs (T(sph)), we could regulate the stiffness of the microcarrier, making the Young's modulus of mTSCs (367.70 ± 79.81 Pa) similar to that of the blastocyst trophoblast ectoderm (432.49 ± 151.90 Pa). Moreover, T(micro) contributes to improve the adhesion rate, expansion area and invasion depth of mTSCs. Further, T(micro) was highly expressed in tissue migration-related genes due to the activation of the Rho-associated coiled-coil containing protein kinase (ROCK) pathway at relatively similar modulus of trophoblast. Overall, our study explores the embryo implantation process with a new perspective, and provides theoretical support for understanding the effect of mechanics on embryo implantation.

1. Introduction

Mechanical signals regulate mouse embryonic developmental processes, which are generated by cell-cell, and cell-microenvironment interactions, with faster feedback and longer propagation distances than biochemical signals [1–4]. Mouse embryo implantation is crucial to the entire study of embryonic development [5–7]. During this process, the trophoblast adheres to the surface of the luminal epithelium and invades the stroma through the basal lamina, achieving cell through interface movement (from blastocyst to uterus) [8,9]. Moreover, trophoblast is strictly regulated by mechanical forces. For instance, differences in contractility on the surface of the blastomere, leading to a distinction between internal and external embryos, demonstrating that contractility

is linked to the positioning of the blastomere and cell fate decisions [10]. In addition, the intraluminal fluid pressure of the blastocyst directly affects trophoblast cell stiffness and division patterns, further regulating trophoblast fate [11]. Unfortunately, it is not clear how mechanics affects trophoblast implantation. Therefore, establishing *in vitro* models to study the mechanics of embryo implantation is crucial.

Currently, trophoblast cells, or mixed with other cells (embryonic, induced, adult stem cells) are used to construct *in vitro* mouse embryo implantation models [12–19]. However, due to the common problem of self-assembly [20–22], these models overlook the role of the mechanical environment, which will cause uncontrollable trophoblast cells stiffness and no significant phenomenon in the through interface cell movement from these models. We know that models for controllable trophoblast

---

cell stiffness have rarely been studied.

The cellular Young's modulus can be regulated by the stiffness of materials [23–25], and the stiffness of the microcarriers regulates stem cell self-renewal and differentiation [26]. Droplet microfluidics technology can generate microcarriers with a homogenous sphere surface and uniform size compared with other methods, such as emulsion-solidification [27–30]. Sodium alginate is a typical natural anionic polymer with high stiffness controllability through molecular weight [31,32]. Therefore, the alginate might be used to regulate the stiffness of microcarriers, which in turn modulates the mechanical properties of trophoblast cells, and to observe their ability to move across the interface.

Here, we constructed alginate microcarriers using droplet microfluidics system. mTSCs could adhere to the surface of microcarriers via modified laminin. Our results show that, compared to T(sph), T(micro) underwent a significant through interface movement process, demonstrated in larger expansion area, greater matrix remodelling, and deeper invasion depth. The variation in mTSC stiffness caused this difference in cell migration. The modulus of mTSCs was similar that of the to trophoblast by regulating the stiffness of microcarriers, activating the RHO/ROCK signaling pathway and promoting through interface movement for mTSCs by regulating cytoskeletal reorganization.

2. Results and discussion

2.1. Droplet microfluidic design and fabrication

The overall experimental process is shown in Fig. 1A. Initially, we designed a microfluidic droplet chip for manufacturing stable and controllable sodium alginate microcarriers (Video S1) (Fig. 1B), and a typical flow-focusing microfluidic structure was used to produce droplets, which achieve a more uniform diameter distribution than other methods [33]. In a water-in-oil-in-oil (w/o/o) emulsion system, sodium alginate mixed with ethylenediaminetetraacetic acid calcium disodium salt (Ca-EDTA), mineral oil, and mineral oil containing acetic acid were added to inlet-1, inlet-2, and inlet-3, respectively, to produce droplets via continuous shear between the water and oil phases. *In situ* crosslinking of Ca^{2+} with sodium alginate was conducted by the diffusion of acetic acid, which prevents the clogging of the chip caused by rapid gelation [34].

Supplementary video related to this article can be found at https://doi.org/10.1016/j.bioactmat.2023.05.007

The concentration and flow rate of the microcarriers were controlled to simulate embryo size. The flow rate ratio of the continuous and dispersed phases was adjusted from 2 to 10. As a result, the droplet diameter was continuously decreased from 107.55 ± 2.4 μm to 79.0 ± 2.9 μm (Fig. 1C and D), and had a coefficient of variation (C.V) lower than 5%, which represents high uniformity. Adjusting the flow rate of the crosslinking phase within a small range did not substantially affect droplet diameter (Fig. S1). Therefore, the diameter of the microcarrier was primarily regulated by the flow rate of the dispersed and continuous phases.

To explore the effect of concentration on the microcarrier size, droplets were prepared using a mixture of 1%–3% sodium alginate and Ca-EDTA at flow rates of 1, 5, and 20 μL/min for the dispersed, continuous, and crosslinking phases, respectively (Fig. 1E). As a result, the diameter of the droplets decreased with increasing concentration from 104.9 ± 2.8 μm to 95.5 ± 3.3 μm (Fig. 1F). Considering that the size of the microcarrier is flexible and conveniently regulated by the flow rate, the droplets were prepared using a mixture of 2% alginate and Ca-EDTA in subsequent experiments without any specific controls. Eventually, we regulated the flow rates (1, 7, and 20 μL/min) to produce embryo sized microcarriers.

2.2. Surface modifications for mTSCs adhesion

Since mammalian cell membranes have no contact sites with sodium alginate [31], the polymer must be modified with a specific protein for mTSCs adhesion. Therefore, we characterized the integrin pairs of mTSCs and found that the highest expression of the adherent integrin
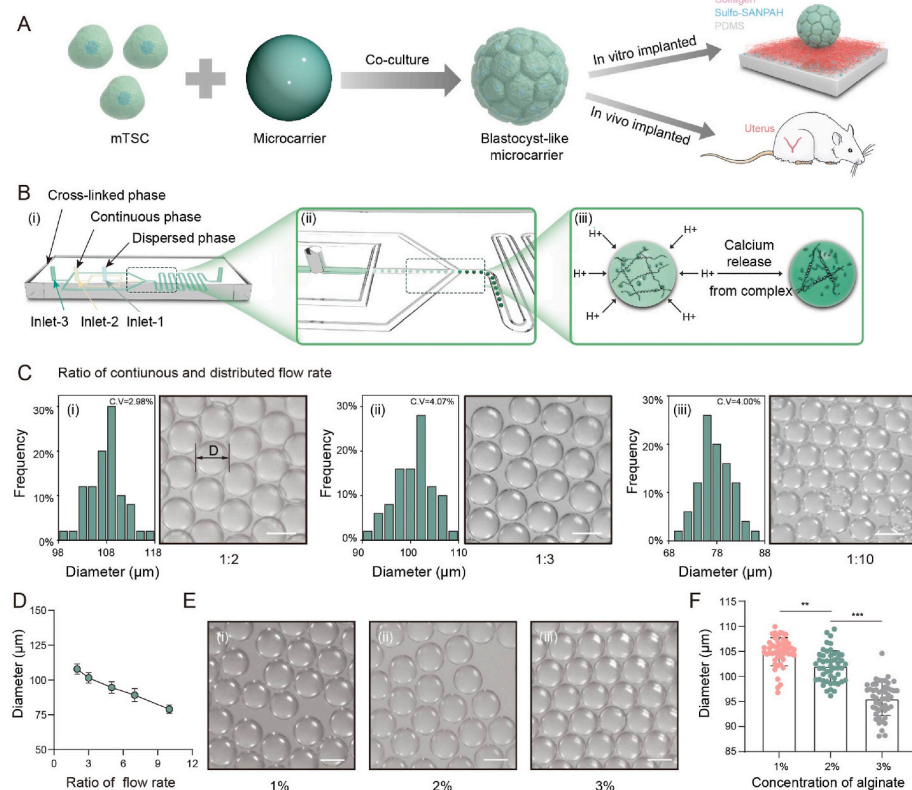

Fig. 1. Design and size control of the droplet microfluidics system. (A) Schematic of the overall process. Microcarriers and mTSCs were mixed and cultured together. After T(micro) formation, they were inoculated into the uterus-like system and pseudopregnant mice, respectively. (B) Schematic of the preparation of microcarriers. (i) Overview of the microfluidic chip. (ii) Schematic of the microcarrier generation at the flow-focusing junction. (iii) Schematic of the crosslinking process. Upon exposure to acid, the Ca-EDTA complex dissolved, releasing calcium ions and inducing alginate crosslinking. (C) Distribution of microcarrier diameter with flow rate ratio, (i), (ii), and (iii) correspond to the distribution and bright field diagram of microcarrier diameters at flow rate ratios of 1:2, 1: 3, and 1:10, respectively. (D) Variation of microcarrier diameter with flow rate ratio (continuous phase/dispersed phase). (E) Bright field diagrams of microcarriers at different concentrations. (i), (ii), and (iii) correspond to alginate concentrations of 1%, 2%, and 3%, respectively. (F) Variation in microcarrier diameter with alginate concentration. All error bars represent ± SD for n = 50 microcarriers per condition. (**P < 0.01, and ***P < 0.001). Scale bars, 100 μm.

pair was laminin (Fig. S2).

To verify the strength of matrix adhesion to mTSCs, a contact test was performed using atomic force microscopy (AFM) probes (Fig. 2A and B). Probes were modified by laminin or collagen, a commonly modified protein used for cell adhesion. A scan of the mTSC surface (Fig. 2C) indicated that the interaction force of laminin (645.7 ± 244.4 pN; Fig. 2D and E) was significantly higher than that of collagen (271.1 ± 83.9 pN; Fig. 2F and G), which was uniformly distributed on the mTSCs surface (Fig. 2H). In summary, the laminin-mTSC interaction force was specific and stronger.

2.3. Establishment of T(micro) model

Based on the adhesion force results, we modified alginate spheres with laminin at concentrations of 0, 5, 25, and 50 μg/mL using carbodiimide chemistry (Fig. S3) and then cultured the microcarrier with mTSCs (Fig. S4) in a 96-well low-adhesion plate to prepare T(micro) (Fig. 3A). We compared laminin modification and evaluated the adhesion status by the contact angle of mTSCs to the microcarrier (Fig. S5) (>90° for good adhesion). As the modification concentration increased, the contact angle increased from 0° to 162.7° ± 11.5° (Fig. 3B), which was greater than that for modified collagen (105.6° ± 27.8°; Fig. 3C). Hence, 50 μg/mL laminin coating microcarriers were used in the subsequent experiments.

Next, we compared T(micro) and T(sph) with E3.5 embryos (Fig. 3D) and found that although there was no differences in diameter (88.8 ± 8.4 μm, 89.3 ± 5.1 μm, and 92.1 ± 6.7 μm, respectively; Fig. 3E) and oxygen consumption rates (OCR) (Fig. S6), T(sph) had more cells (103.4 ± 16.7) than T(micro) (31.2 ± 3.3) and E3.5 (30.8 ± 2.9; Fig. 3F). Moreover, CDX2 (a trophoblast transcription factor)

immunofluorescence staining indicated that the distribution of cells on T (micro) was more similar to that of E3.5, while T(sph) just resembled a cluster of cells (Fig. 3G and H).

We performed RNA sequencing to further investigate the transcriptome characteristics of T(micro) and T(sph) compared to those of E3.5 (Fig. S7). Differences in cell types can significantly increase the variation in transcriptome features; thus, we mainly compare T(micro) and T(sph). T(micro) and T(sph) RNA sequencing analysis revealed that mTSCs on T(micro) exhibited an increasing trend for some maintaining stemness-related genes compared with T(sph), including *Eomes*, *Elf5*, and *Esrrb* (Fig. S8), and we noticed that mTSCs differentiation genes such as *Hand1*, *Mdfi*, *Ascl2*, and *Egfr* [35] were more highly expressed in T(sph). In summary, we suggest that mTSCs on T(micro) are more similar to blastocyst trophoblast cells in terms of number, morphology, and trends of stemness-related genes.

2.4. T(micro) exhibits higher implantability on a uterus-inspired niche (UN) system

Trophoblast cells undergo a significant through-interface movement process during embryo implantation in mice [9]. Based on this, T(micro) and T(sph) were inoculated on UN (Video S2), a mimic uterus platform to support mouse embryo implantation and development [36], and we found that T(micro) had a higher adhesion efficiency (80%) and larger percentage of the mTSC expansion area (5.95 ± 1.85) than T(sph) (24%; 1.89 ± 0.66; Fig. 4A–C). Interestingly, after inoculation onto the UN, some of the T(sph)s expanded in 2D fashion, losing conventional spherical characteristics. The reason for this phenomenon is not clear (Fig. 4A). Next, we used specific antibodies against collagen I to label the structure of collagen and observed a significant migration of the mTSCs
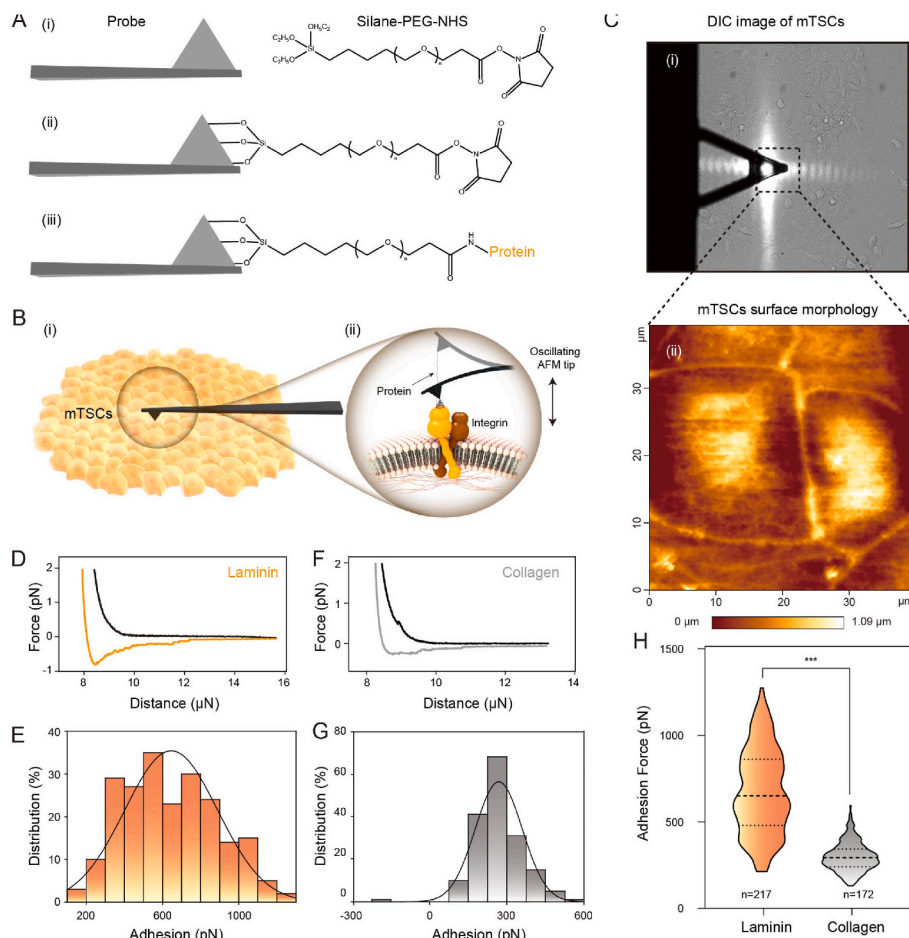

Fig. 2. Microcarrier surface modification for mTSCs attachment. (A) Schematic of AFM probe modifications. (i), (ii), and (iii) indicate the methods for binding the probe to silane-PEG-NHS and protein (laminin or collagen). (B) Schematic of the probe contact with cells. (i) Overview of the probe scanning mode. (ii) Partially zoomed diagram. The probe pulls the integrin pairs through proteins. (C) Image of the AFM probe scanning mTSCs. (i) Differential interference contrast (DIC) images of mTSCs during AFM test. (ii) Image of the mTSC surface morphology. (D to H) Contact force of laminin and collagen with mTSCs. (D and F) Force–Distance curves of laminin and collagen, respectively. (E and G) Distribution of adhesion force of laminin and collagen, respectively. (H) Statistical diagram of the differences in adhesion force. n > 150 adhesion force curves per condition. (***P < 0.001).
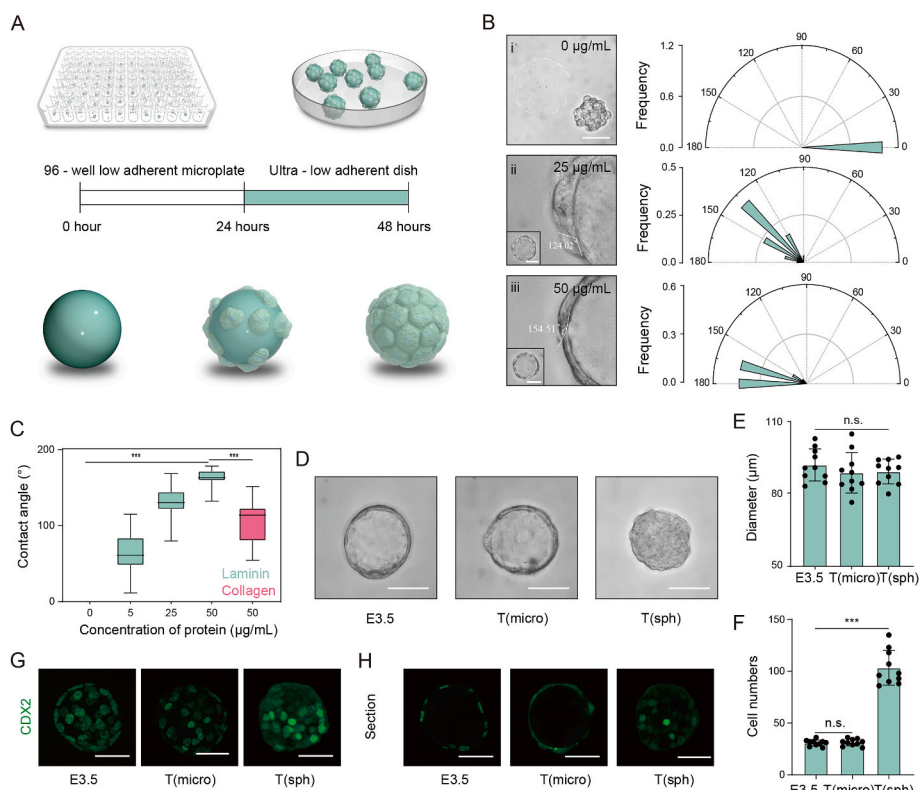
Fig. 3. Preparation and biological characterization of T(micro). (A) Schematic for the preparation of T(micro). (B) Bright field (left) and angular distribution of mTSCs adhesion for modifications (right) under different concentrations. (i), (ii), and (iii) indicate modification with 0, 25, and 50 μg/mL laminin, respectively. (C) Cell angle statistics for modifying different concentrations of laminin, and collagen (50 μg/mL), error bars represent ± SD for n = 30 cell contact angles per condition. (***$P <$ 0.001). (D) E3.5, T(micro), and T(sph) in bright field. (E and F) T(micro) and T(sph) compared with E3.5 in diameter and cell number, ±SD for n = 10 diameter and cell number per condition. (***$P <$ 0.001). (G and H) Immunofluorescent (IF) comparison of E3.5 with T(micro) and T(sph) in (G) maximum intensity projection image and (H) maximum cross section image. Scale bars, 50 μm.

from T(micro) on the fourth day, while T(sph) only expanded in volume (Fig. 4D). We also observed lower levels of the epithelial biomarker E-cadherin (E-cad; 49.06 ± 15.25 A.U.) compared to T(sph) (102.66 ± 19.78 A.U.; Figs. S9A and B), indicating the occurrence of epithelial-mesenchymal transition (EMT), which plays an essential role in the regulation of trophoblast migration and invasion [37,38]. Scanning electron microscopy (SEM) images showed that mTSCs on T(micro) spread radially on collagen. The collagen fibers were strained at the interface between the material and the cells (Fig. 4E). In contrast, T(sph) on collagen showed smooth expanding outer edges without visible microvilli-like structures.

Supplementary video related to this article can be found at https://doi.org/10.1016/j.bioactmat.2023.05.007

Mouse embryo implantation is accompanied by drastic ECM remodelling [38]. Using Imaris 9.0.2 for collagen and nucleus region selection at the vertical level, we observed cell invasion in the collagen (Fig. 4F and G, Video S3). T(micro) displayed deeper invasion (39.22 ± 6.48 μm) than T(sph) (20.72 ± 3.51 μm). Moreover, T(micro) exhibited higher fluorescent expression (64.91 ± 17.89 A.U.) to T(sph) in matrix metalloproteinase-9 (MMP-9) (16.70 ± 9.54 A.U.; Figs. S9C and D), which plays an important role in the breakdown and remodelling of ECM proteins [39], further supporting the notion that T(micro) reshapes the collagen network structure. These results demonstrated that significant through-interface movement occurred in UN's T(micro) (Fig. 4H).

Supplementary video related to this article can be found at https://doi.org/10.1016/j.bioactmat.2023.05.007

In vivo implantation experiments were also performed. T(micro), T(sph), and cell-free microcarriers were transplanted into pseudopregnant mice (Fig. S10). After 4 days, both T(micro) and microcarriers had implantation sites and decidua formation that were not present in the uterus transplanted with T(sph). This demonstrates that the microcarriers can improve the implantation efficiency of mTSCs.

2.5. T(micro) facilitates the migration of mTSCs on the microcarrier

To explore the cause of the implantability differences, we compared the gene ontology biological process (GO-BP) analysis of T(micro) and T(sph) before and after inoculation to the UN system (Fig. S11). GO-BP analysis revealed that the upregulated genes in T(micro) were enriched in associated with tissue migration and regulation of MAP kinase activity. Similarly, these migration-associated genes were upregulated in T(micro) on collagen after culture for two days (Fig. 5A), with the genes differing from those in the earlier period. As ROCK is a Rho-GTPase effector of actin cytoskeleton control, which plays a key role in cell movement [40], the addition of the ROCK inhibitor Y27632 (Y; Fig. S12) (Fig. 5B), the adherence efficiency did not change much (DMSO, 78%; Y, 60%; Fig. 5C), but the percentage of the mTSCs expansion area was significantly reduced (DMSO, 7.78 ± 1.30; Y, 2.53 ± 0.51; Fig. 5D), which led to the decreased pulling of the fibrils by the mTSCs (Fig. 5E) as well as a reduced invasion depth (DMSO, 40.287 ± 4.814 μm; Y, 17.82 ± 3.74 μm; Fig. 5F, G) and supported the authenticity of the GO analysis

We also found that T(micro) on collagen upregulated the expression of matrix adhesion-related genes (Fig. 5A). Moreover, the IF marker for focal adhesion kinase (FAK), a mechanosensor of tissue rigidity [41], revealed the presence of cellular pseudopods in T(micro), which was not observed in T(sph) (Fig. S13). This phenomenon is similar to the remodelling of collagen fibres by mTSC on T(micro) (Fig. 4E).

2.6. Stiffness promoting implantation of mTSCs

Stiffness can induce and regulate cell motility via ROCK-mediated mechanisms [42,43]. Thus, we hypothesized that the stiffness of the mTSCs in T(micro) affects their expansion area, matrix remodelling, and invasion depth.

Firstly, using AFM tests, we found that the modulus of mTSCs was similar to that of trophoblast (432.49 ± 151.90 Pa) on T(micro) (367.70 ± 79.81 Pa) and lower on T(sph) (120.39 ± 33.37 Pa; Fig. 6A), and its
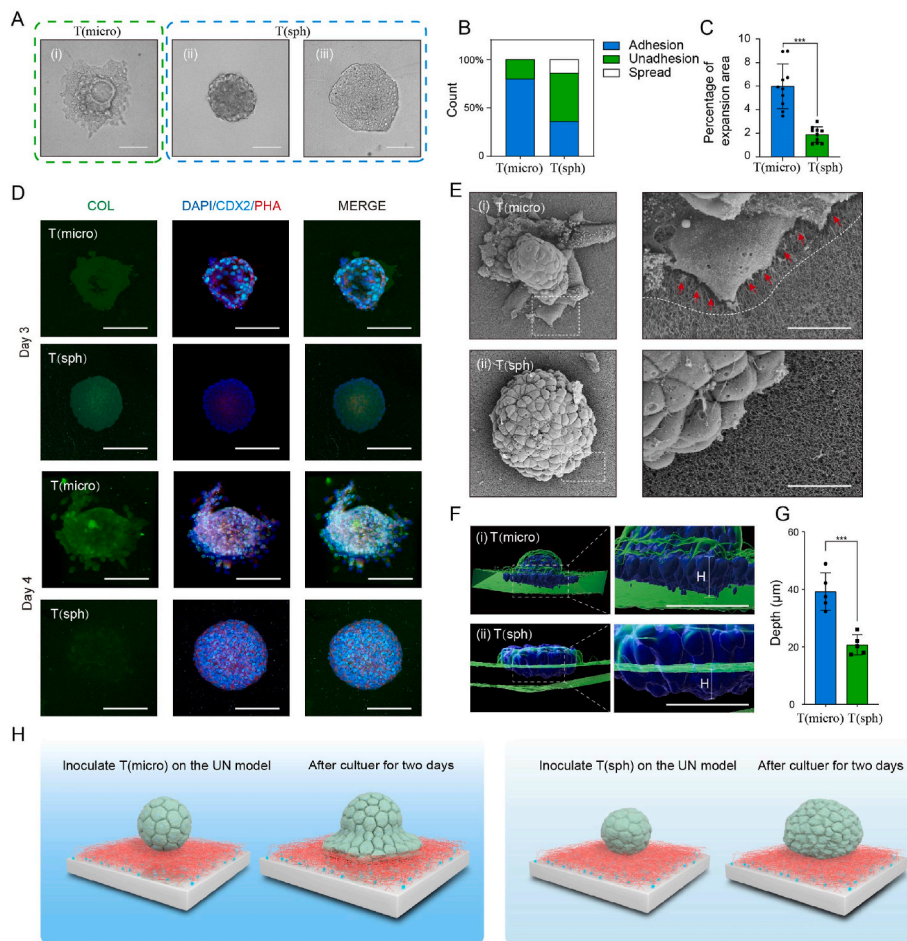
Fig. 4. T(micro) can enhance the implantability of mTSCs on UN. (A) Bright field diagram showing T(micro) and T(sph) inoculated on UN. (i) T(micro) images of the fourth day. (ii) and (iii) show two types of result graphs for T(sph) on the fourth day. (B) T(micro) and T(sph) adherence rates, n = 50. (C) Statistical analysis of the percentage of expansion area on T(micro) and T(sph), error bars represent + SD for n = 10 new area rates per condition. (D) IF images over time in T(micro) and T(sph) on UN. (E) SEM images of T(micro) and T(sph) on collagen. The right images are zoomed in on the left images. Red arrows indicate remodelled collagen fibres, scale bars, 30 μm. (F) Regions showing collagen (green) and the cell nucleus (blue). Right images are zoomed in on the left images. Scale bars, 50 μm. (G) Statistical diagram of invasion distance for T(micro) and T(sph), n = 5. (H) Schematic of the inoculation of T(micro) and T(sph) on UN. Compared with T(sph) (right), T(micro) (left) demonstrated greater implantation capability, with a larger expansion area and deeper invasion depth. (***$P < 0.001$). Scale bars, 100 μm.

modulus was reduced via the addition of ROCK inhibitors (96.34 ± 18.32 Pa; Fig. 6B). Moreover, we prepared a lower molecular weight (MW) alginate by irradiation with a cobalt source (Table S1), which reduced the stiffness of the alginate hydrogel (Fig. 6C). The moduli of mTSCs decreased (301.27 ± 103.78 Pa; Fig. 6D) with reduced through interface movement characteristics (Fig. 6E), although there was little change in adhesion efficiency (75%; Fig. 6F), including a decrease in the expansion area (3.78 ± 0.76; Fig. 6G), pulling fibers (Fig. 6H) and invasion distance (29.63 ± 4.48 μm; Fig. 6I and J) when seeded on the surface of the microcarriers (L-micro) as mentioned above. As a result, the microcarriers provided more similar stiffness support to the trophoblast and increased ROCK activity, which facilitates mTSC's implantation capability.

In vitro models play a crucial role in studying the mechanics of embryo implantation . However, previous models have overlooked the adjustment of trophoblast hardness, likely due to challenges associated with the random self-assembly of stem cells. We selected T(sph) formed by mTSCs self-assembly, similar in size to E3.5, and found that the modulus of mTSCs in T(sph) was significantly lower than that of the E3.5 trophoblast. Moreover, there were inconspicuous through-interface movement phenomena in this model during implantation.

In this study, we prepared stiffness-changed microcarriers with droplet microfluidics, which produce a more uniform diameter distribution than other methods [20]. Using transcriptome analysis and adhesion testing, we determined that laminin is an ECM niche for mTSCs, consistent with previous reports [44,45]. This model has a more similar cell arrangement and modulus to the blastocyst compared with the T(sph) model. Moreover, our model demonstrates greater implantation capability on a uterus-inspired niche system, a good platform for

observing embryo implantation [46], and higher implantation efficiency *in vivo*. When ROCK inhibitors were added and the MW of the microcarrier decreased, the implantation phenomena decreased, similar to the "durotaxis" movement of most tumor cells [42,47]. In comparison, our model has two advantages: modulation of mTSCs mechanical properties by microcarrier stiffness and overcoming the contradiction between random stem cell self-assembly and the trophoblast regulation by strict mechanical control; mTSCs with similar stiffness to the trophoblast exhibit faster movements than T(sph), consistent with previous research in other cells [48,49].

The limitation of our study is that we cannot add additional variables, such as inner-cell mass (ICM) and endometrial epithelial layer, to explain the impact of the mechanical properties of the trophoblast on embryo implantation. However, future studies utilizing hollow microcarriers with ICM and a mimetic uterine platform containing the endometrial epithelial layer may further improve the implantability and developmental capacity of T(micro).

3. Conclusions

We used droplet microfluidics to construct a trophoblast implantation model with variable stiffness. This model exhibited similar cell number, morphological distribution, and cellular stiffness to that of mouse blastoderm trophoblast. By adjusting the modulus of the microcarrier, we were able to modulate the stiffness of the mTSCs on their surface. mTSCs on microcarriers demonstrated higher implantation capacity at similar stiffness to the trophoblast, activating the RHO/ROCK signaling pathway and promoting interface movement through regulating cytoskeletal reorganization. This suggests that the mTSC
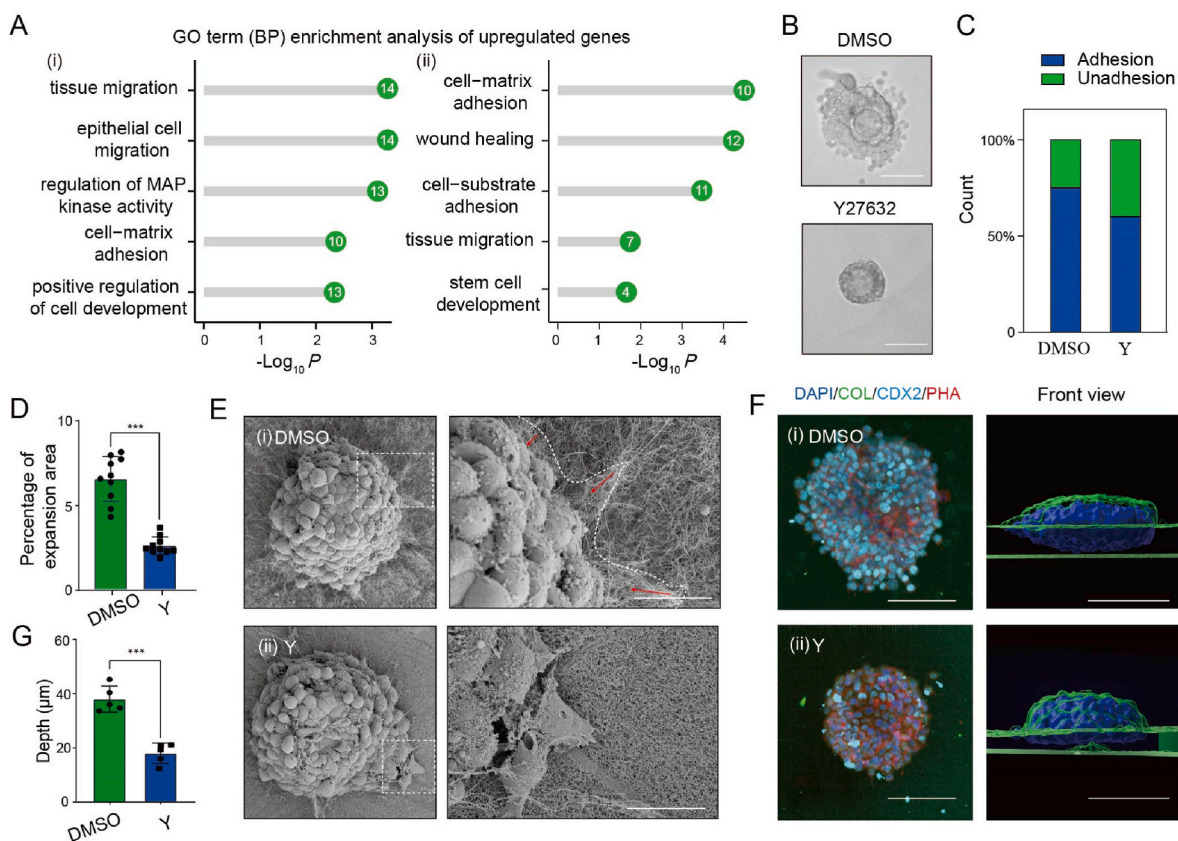
Fig. 5. Effect of T(micro) on the migration capability of mTSCs. (A) GO enrichment analysis of upregulated genes in (i) T(micro) vs T(sph) and (ii) T(micro) on collagen vs T(sph) on collagen. The number of enriched genes in each GO term is shown in circles. (B) Bright field plots of DMSO and Y27632 added on collagen with medium, scale bars, 100 μm. (C) DMSO and Y adherence rates, n = 50. (D) Statistical analysis of the percentage of expansion area on DMSO and Y, error bars represent ± SD for n = 10 new area rates per condition. (E) SEM images of DMSO (i) and Y (ii) on collagen. Right images are zoomed in the left images, red arrows indicate remodelled collagen fibres, scale bars, 20 μm. (F) IF plots and (ii) region identification of DMSO (i) and Y (ii); green represents collagen, and blue represents the nucleus. Statistical diagrams of invasion distances for (G) DMSO and Y, ±SD for n = 5 depth condition. Scale bars, 100 μm. (***$P < 0.001$).

implantation capability can be regulated, which enhances our understanding of embryo implantation from a biomechanical perspective and provides a criterion for evaluating embryo implantation capacity *in vivo*.

4. Experimental section

4.1. Chip design and photolithography

The layout of the microfluidic chips was designed using SolidWorks software (Dassault Systemes, SolidWorks, USA). First, a 500 nm thick negative photoresist (SU-8 2050.5, MicroChem, USA) was spin-coated onto a 4-inch silicon wafer and soft-baked for 5 min at 95 °C. The film mask was then placed onto the wafer, exposed to ultraviolet (UV) light to induce polymerization and post-baked at 95 °C for 5 min. To remove the uncross-linked photoresist, a master was developed using propylene glycol methyl ether acetate.

A 10:1 ratio of elastomer Polydimethylsiloxane (PDMS) to curing agent (SYLGARD 184, Dow Corning, USA) was used to fabricate microfluidic devices. The mixture was cured for 4 h at 60 °C. The hardened PDMS was then cut and peeled off the master, and 1 mm holes were punched into the PDMS. This was then bonded onto a glass slide via treatment with a plasma bonder (Diener Electronic, Ebhausen, Germany). Finally, the channels were modified with trimethoxy (1H, 1H, 2H, and 2H-heptadecafluorodecyl) to create a hydrophobic surface before the chip was used.

4.2. Droplet formation and modification

The flow rates within the channels were controlled using a Harvard syringe pump (Pump 11, Pico Plus, USA). The microcarrier was prepared as described previously [34]. Briefly, the Ca-EDTA complex was prepared by mixing a solution of 100 mM calcium chloride ($CaCl_2$) with a solution of 100 mM EDTA in equal ratios. The pH of the Ca-EDTA solution was adjusted to approximately 7 by adding sodium hydroxide. Sodium alginate (A2033, Sigma-Aldrich, USA) was dissolved in 0.9% sodium chloride (NaCl). 1%, 2%, and 3% w/v sodium alginate was then mixed with the Ca-EDTA solution at an equal ratio and used as the dispersed phase. Mineral oil (M5904, Sigma-Aldrich, USA), containing 2% v/v Span 80 (85548, Sigma-Aldrich, USA), was used as the continuous phase. The crosslinked phase was mineral oil with 2% v/v Span 80 and 0.1% v/v acetic acid (A6283, Sigma-Aldrich, USA). After generation, the microcarriers were rinsed with Hank's balanced salt solution (14025-092, Gibco, USA) and centrifuged. Subsequently, the alginate microcarriers were coated with 200 mM 1-(3-dimethylaminopropyl)-3-ethylcarbodiimide hydrochloride (EDC; E7750, Sigma-Aldrich, USA) and 50 mM N-hydroxy succinimide (NHS; 130672, Sigma-Aldrich, USA) for 90 min at room temperature (RT). Subsequently, the microcarriers were washed thrice with Hanks' solution and incubated in 0, 5, 25, 50 μg/mL laminin (23017015, Gibco, USA) or 50 μg/mL type I collagen (5133, Advanced BioMatrix, USA) overnight at 4 °C. After activation, the microcarriers were washed three times with Hanks' solution and cultured in cells.
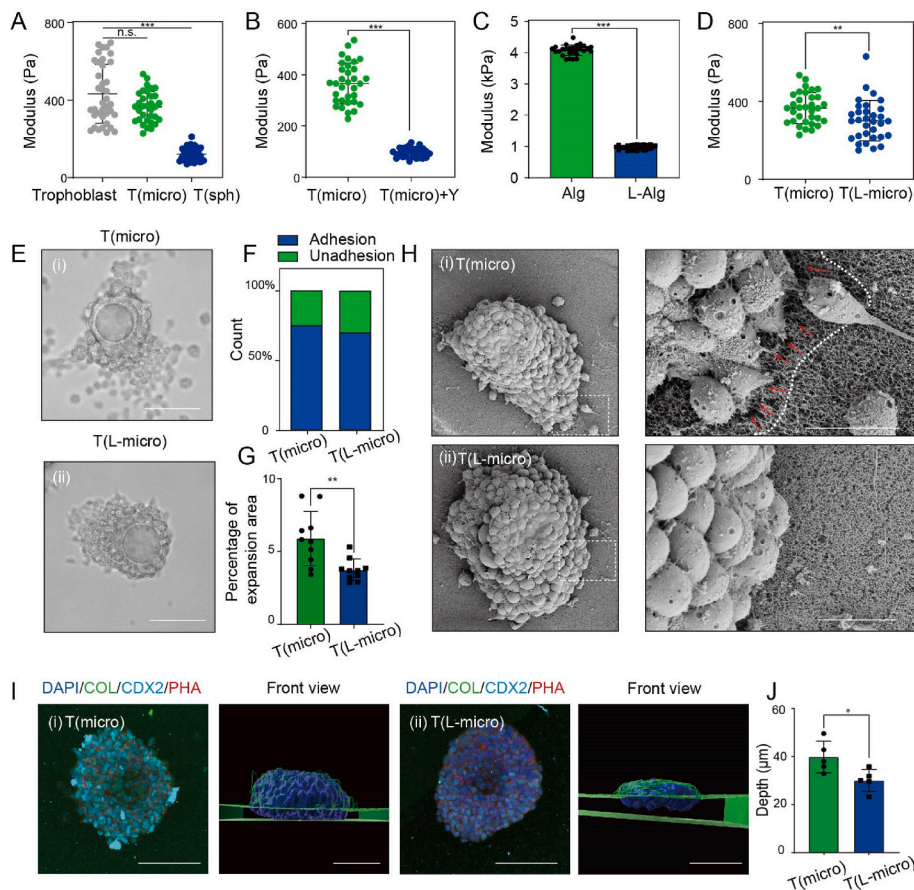
Fig. 6. Effect of stiffness on the implantability of mTSCs. (A) Modulus statistics plot for trophoblast, T (micro), and T(sph), ±SD for n > 30 adhesion force curves per condition. (B) Comparison between the modulus of T(micro) and T(micro)+Y, n > 30 moduli per condition. (C) Modulus of Alg and L-Alg by nanoindentation. ± SD for n = 27 moduli per condition. (D) Comparison between the modulus of T (micro) and T(L-micro), n > 30 moduli per condition. (E) Bright-field plots of T(micro) and T(L-micro) added on collagen with medium, scale bars, 100 μm. (F) T(micro) and T(L-micro) adherence rates, n = 50. (G) Statistical analysis of the percentage of expansion area on T(micro) and T(L-micro), error bars represent + SD for n = 10 new area rates per condition. (H) SEM images of T(micro) (i) and T(L-micro) (ii) on collagen. Right images are zoomed in on the left images. Red arrows indicate remodelled collagen fibres, scale bars, 20 μm. (H) IF plots and (ii) region identification of T(micro) (i) and T(L-micro) (ii); green represents collagen, and blue represents the nucleus. Statistical diagrams of invasion distances for (I) T(micro) and T(L-micro), ±SD for n = 5 depth per condition. Scale bars, 100 μm. (*$P < 0.05$, **$P < 0.01$, and ***$P < 0.001$).

4.3. mTSC culture

mTSCs were obtained from the Zhou laboratory (Institute of Zoology, Chinese Academy of Sciences, Beijing, China) and isolated from the mouse blastocyst [50]. Briefly, there were four steps, prepare 4-well plates of mouse embryonic fibroblasts, collect blastocysts, disaggregate blastocyst outgrowths and isolate mTSC colonies. mTSCs were grown as previously described [51], at 37 °C in 95% air and 5% CO$_2$. mTSCs medium contained 20% fetal bovine serum (FBS; 04-001-1A, Biological Industries, Israel), 1 mM sodium pyruvate (11360-070, Gibco, USA), 50 μg/mL penicillin/streptomycin, $5.5 \times 1\,0^{-5}$ M β-mercaptoethanol (21985023, Gibco, USA), 25 ng/mL basic fibroblast growth factor (FGF4) (AF-100-31, PeproTech, USA), and 1 μg/mL heparin (07980, Stemcell, Canada) in RPMI 1640 (11875-093, Gibco, USA), with 70% of the medium preconditioned (mTSC culture medium without heparin and FGF4) by incubation with embryonic fibroblasts for 72 h.

4.4. Embryo recovery

ICR 7- to 8-week-old female and 8-week-old male mice were purchased from SPF Biotechnology (Beijing, China). ICR mice were raised under specific-pathogen-free conditions and handled following the Animal Care and Use Committee guidelines of the Institute of Zoology, Chinese Academy of Sciences (ethical approval no. IOZ20190068). Pregnant mice were humanely euthanized 3.5 days post coitum through cervical dislocation, and the embryos were flushed out with flush medium containing CMRL 1066 (11530-037, Gibco, USA), 5 × penicillin-streptomycin (60162ES76, Yeasen, China), and 10% FBS.

4.5. Analysis of chromosome ploidy

Chromosomal ploidy was conducted: Step 1: mTSCs were collected via centrifugation at 1200 rpm (3 min, 4 °C). Step 2: Cells were resuspended with 70% ethanol overnight (4 °C). Step 3: Cells were centrifuged and washed once with PBS. Step 4: Cells were resuspended with 1 mg/mL RNase (60 min, 37 °C). Step 5: Cells were filtered using a 40 μm cell strainer. Step 6: Cells were resuspended with 10 μg/mL Hoechst (H3570, Invitrogen, USA) in the dark (30 min, 37 °C). Step 7: Samples were measured using flow cytometry (BD LSRFortessaTM × -20, BD Biosciences, USA), and FlowJo 10.8.1 was used for data analysis.

4.6. Preparation and culture of T(micro) and T(sph)

20 cells and single microcarriers were added to 96-well low-cell-adhesion plates (7007, Corning, USA) to obtain T(micro), or 100 cells were added to obtain T(sph). Cells and microcarriers are added to the plate with a mouth pipette, and both T(micro) and T(sph) were cultured in 50 μL mTSC media and then centrifuged at 1000 rpm to facilitate aggregation between cells and microcarriers or cell-to-cell. T(micro) or T(sph) were transferred to a 6 cm low cell-adhesion dish coated with 1% agarose (111860, Biowest, France) after 12 h. The day the cells were seeded in the 96-well low-cell-adhesion plates was defined as day 0.

4.7. Contact angle measurement

The contact angle was measured by quartering the microcarrier and measuring the cells in each corner to ensure the randomness and authenticity of the data. Each concentration measurement is at no less than eight microcarriers.

4.8. OCR testing

5-chloromethyl fluorescein diacetate (CMFDA) (40721ES50, Yeasen, China) was used to monitor OCR. Briefly, T(micro) and T(sph) were cultured in TS medium with 10 μM CMFDA for 30 min, then washed three times with PBS, and cultured in fresh TS medium for 30 min. Zeiss LSM880 confocal microscope was then used to image each sample.

4.9. Fabrication of the UN system

The UN system was prepared as described previously [36]. Briefly, PDMS was made by a 10:1 mixture of PDMS base and a curing agent was poured into the four-well plate. Each well received 0.2 g PDMS and was cured for 4 h at 60 °C before being processed under a 30 W plasma for 5 min. The PDMS surface was pretreated with 0.2 mg/mL sulfo-SANPAH (22589, Thermo Fisher Scientific, USA) and coated overnight with 50 μg/mL collagen. Collagen (7.5 mg/mL) was added to the coated PDMS wells and cured at 37 °C for 1 h. T(micro) and T(sph) were seeded onto the UN by mouth pipette.

4.10. In vitro and in vivo implantation

T(micro) and T(sph) were added to the UN by mouth pipette. The adhesion was observed after one day of incubation. For samples that adhered and spread, the spread ability was characterized by the ratio of the new area to the initial area after two days culture. Ten samples were statistics with each case.

In order to get pseudopregnant mice, ICR female mouse copulation with a vasectomized male, and to test for manifestations of hormonal pregnancy. T(micro), T(sph), and microcarriers were transplanted into pseudopregnant mice used a mouth pipette. The mice were sacrificed four days after transplantation. Before obtaining the uterus, intravenous injections injected 0.1% trypan blue (T6146, Sigma-Aldrich, USA) into the mice. Then uterus was removed, and the implantation site and decidua area were calculated. Three mice were transplanted with each condition in a unilateral uterus. Thirty samples were transplanted for each condition.

4.11. Inhibitor experiments

After mixing 20 mTSCs and a microcarrier in the plate, add DMSO and 5, 10, 20, 50 μM of Y27632 (S1049, Selleck, USA) in medium, respectively. Observe the cell adhesion status after 48 h of culture.

4.12. AFM mechanical testing

To test the adhesion of collagen/laminin to mTSCs, we modified collagen/laminin on the MLCT-BIO-D probe, as described previously [52]. The probes were cleaned under 30 W plasma for 5 min, followed by 1 mM silane-PEG-NHS (20,000 Da) and 4 mM EDC (DMSO as solvent) for 2 h at RT. The cells were washed three times with phosphate-buffered saline (PBS). After that, probes were washed using collagen/laminin overnight at 4 °C.

Contact mode force spectroscopy was used for adhesion testing using a JPK NanoWizard 4. mTSCs were seeded in 60 mm culture dishes. The test was performed at a scanning speed of 2 μm/s, with a loading force of 2 nN at a z-length of 8 μm, and collagen/laminin was allowed to contact mTSCs for 10 s mTSC Young's modulus (in the follow-up, called modulus) was tested using JPK NanoWizard 4 and NP-O10 probes attached to a microsphere (9030, Thermo Fisher Scientific, USA). For the embryo samples, we cultured E3.5 embryos in culture dishes containing agarose to prevent the embryo adhesion. After 0.5–1 days of *in vitro* culture until the zona pellucida spontaneously detached, then used to test. All samples were half-embedded in agarose on 60 mm culture dishes. The test was performed at a z-speed of 2 μm/s with a setpoint of 2 nN and a z-length of 2 μm. For each force curve, JPKSPM data

processing was used for data analysis.

4.13. Preparation of low-MW alginate

Briefly, low-MW alginate was prepared by irradiating alginate with a 5 Mrad cobalt source. The MW distributions of the alginates were determined using gel permeation chromatography (Waters Breeze™ 2, Waters, USA). The samples were dissolved in water for a concentration of 3 mg/mL, and 200 μL of the sample was injected into the instrument. Glucan standards were used for molecular weight calculations, and the weight-average MW was used.

4.14. Hydrogel mechanical testing

A nano-indenter instrument (Piuma; Optics11, Netherlands) was used to determine the alginate hydrogel stiffness. Alginate hydrogel was formed using alginate and Ca-EDTA at pH 7.0 and then mixed at a 2:1 ratio with an aqueous solution of D-glucono-δ-lactone (G4750, Sigma-Aldrich, USA). All samples were measured using a probe with a radius of 38 μm and a cantilever stiffness of 0.3 N/m. Cantilever bending calibrations were performed before each series of experiments by indenting a rigid surface beneath it. Each sample was tested (3×3 matrix) in a 300×300 μm grid scan with 100 μm between measurement areas. The indentation protocol comprised a loading phase for 2 s at an indentation depth of 10 000 nm, which was held for 1 s, and then an unloading phase for 2 s. JPKSPM data processing was used for data analysis. More than three experiments were conducted for each mechanically tested sample for reliability analysis.

4.15. IF staining

E3.5, T(micro) and T(sph) are collected by mouth pipette, other samples are collected from a four-well plate directly. Samples were washed thrice with PBS at RT, fixed with 4% paraformaldehyde overnight (4 °C), and washed three times with PBS at RT. Cells were then permeabilized with 1% Triton X-100 in PBS for 4 h at RT, then blocked with 0.1% Tween-20, 0.01% Triton X-100, and 3% BSA in PBS overnight (4 °C). Thereafter, primary antibodies against CDX2 (3977S, Cell Signaling Technology, USA), SOX2 (3977S, Cell Signaling Technology), collagen I (ab90395, Abcam, UK), laminin (ab11575, Abcam, UK), E-cadherin (3195S, Cell Signaling Technology, USA), and phosphor-FAK (44-624G, Invitrogen, USA) were diluted in a blocking solution (1:100) and incubated with cells overnight (4 °C). Samples were then washed with 0.1% Tween-20 and 0.01% Triton X-100 in PBS three times for 20 min at RT, followed by overnight incubation (at 4 °C) with appropriately diluted secondary antibodies (1:500) in the wash solution. The secondary antibodies used were Alexa 488 donkey anti-mouse (A21202, Invitrogen, USA), 488 goat anti-rabbit (A11034, Invitrogen, USA), Cyanine3 goat anti-mouse (A10521, Invitrogen, USA), and Cyanine3 goat anti-rabbit (A10520, Invitrogen, USA). Samples were washed thrice for 20 min at RT using the wash solution. Next, 10 μg/mL Hoechst (1:1000 dilution) and phalloidin (40762ES75, Yeasen, China) solutions (1:100) were prepared and incubated with samples for 20 min at RT. Finally, the samples were washed thrice for 20 min at RT and clarified using 1.3 g/mL histodenz (D2158, Sigma-Aldrich, USA) to increase luminosity (for the UN system). Subsequently, all samples were imaged using a Zeiss LSM880 confocal microscope. Imaris 9.0.2 software was used to construct the 3D images.

4.16. SEM imaging

For SEM, we began by fixing samples with 2.5% glutaraldehyde overnight at 4 °C. Samples were then dehydrated in 30%, 40%, 50%, 60%, 70%, 80%, and 90% ethanol for 15 min each, followed by dehydration in 100% ethanol three times. Dry samples were subjected to supercritical drying (aotosamdri-815, Tousimis, USA), then sprayed

with platinum (JEC-3000FC, JEOL, Japan). Finally, samples were observed using SEM (SU8010, Hitachi, Japan).

4.17. Fourier transform infrared spectroscopy (FTIR)

A spectrophotometer (NicoletTM iS50, Thermo Fisher Scientific, USA) was used to record the FTIR spectra of the microcarriers in the wave number range from 4000 to 500 cm^{-1}, using the attenuated total reflectance (ATR) module with a resolution of 4 cm^{-1} and 32 scans.

4.18. Live cell imaging

Live cell imaging was performed using the CytoSMART system (CytoSMART, Lux2, Netherlands). The shooting gap was 10 min, the duration was 2 days, and the pictures were continuously collected to form the MP4 video.

4.19. RNA-seq analysis

All samples are added to the lysis buffer by mouth pipette after 3 times wash with PBS at 4 °C. The Annoroad Gene Technology Corporation constructed the whole transcriptome libraries and the sequencing. Next, FastQC (v0.11.5; http://www.bioinformatics.babraham.ac.uk/projects/fastqc/) was used to determine the sequencing reading quality. Next, we used HISAT2 to align the clean reads to the GRCm38 reference genome software (v2.2.1) [53]. The FeatureCounts software (v1.6.3) [54] was used to determine the transcriptional expression levels of each gene. Differentially expressed genes (DEGs) were calculated in the bio-conductor using the R package DESeq2 (v1.32.0) [55]]with a cutoff p-adjusted value < 0.05 and Log2 (fold change) > 1. The EnrichGO function from the R package clusterProfiler (v4.0.2) [56] was used for GO enrichment analysis to determine the over-represented pathways and GO terms of the DEGs. The R packages ggplot2 (v3.2.1; https://ggplot2.tidyverse.org) and Pheatmap (v1.0.12; https://cran.r-project.org) were used to visualize results.

4.20. Statistical analysis

Statistical analyses were performed using GraphPad Prism 9 and Origin 9. Diameter, angle, area, and MFI were measured using ImageJ software. Cell numbers were counted using Imaris 9.0.2. Data are presented as the mean ± SD. The *t*-test and one-way ANOVA were used to analyze the statistical significance of two and three or more data groups.

CRediT authorship contribution statement

Zili Gao: Writing – original draft, designed the microfluidic chips, performed the experiments, Formal analysis, Writing – original draft. **Jia Guo:** Methodology. **Bo Gou:** Formal analysis. **Zhen Gu:** Writing – original draft, All authors discussed the results. **Tan Jia:** performed the experiments. **Sinan Ma:** performed the experiments. **Liyuan Jiang:** provided the mouse trophoblast stem cells. **Wenli Liu:** designed the microfluidic chips. **Lixun Zhou:** designed the microfluidic chips. **Qi Gu:** Methodology.

Declaration of competing interest

Qi Gu is an editorial board member for Bioactive Materials and was not involved in the editorial review or the decision to publish this article. The authors declare that they have no competing interests.

Acknowledgements

Appendix A. Supplementary data

Supplementary data to this article can be found online at https://doi.org/10.1016/j.bioactmat.2023.05.007.

References

[1] J.H. Shawky, L.A. Davidson, Tissue mechanics and adhesion during embryo development, Dev. Biol. 401 (2015) 152–164, https://doi.org/10.1016/j.ydbio.2014.12.005.

[2] K.H. Vining, D.J. Mooney, Mechanical forces direct stem cell behaviour in development and regeneration, Nat. Rev. Mol. Cell Biol. 18 (2017) 728–742, https://doi.org/10.1038/nrm.2017.108.

[3] J.-L. Maître, Mechanics of blastocyst morphogenesis, Biol. Cell. 109 (2017) 323–338, https://doi.org/10.1111/boc.201700029.

[4] J.-L. Maître, R. Niwayama, H. Turlier, F. Nédélec, T. Hiiragi, Pulsatile cell-autonomous contractility drives compaction in the mouse embryo, Nat. Cell Biol. 17 (2015) 849–855, https://doi.org/10.1038/ncb3185.

[5] A. Weberling, M. Zernicka-Goetz, Trophectoderm mechanics direct epiblast shape upon embryo implantation, Cell Rep. 34 (2021), 108655, https://doi.org/10.1016/j.celrep.2020.108655.

[6] J. Cha, X. Sun, S.K. Dey, Mechanisms of implantation: strategies for successful pregnancy, Nat. Med. 18 (2012) 1754–1767, https://doi.org/10.1038/nm.3012.

[7] K. Su-Mi, K. Jong-Soo, A review of mechanisms of implantation, J. Reprod. Dev. 21 (2017) 351–359, https://doi.org/10.12717/DR.2017.21.4.351.

[8] M.N. Fukuda, K. Sugihara, Cell adhesion molecules in human embryo implantation, Sheng Li Xue Bao 64 (2012) 247–258.

[9] H. Wang, S.K. Dey, Roadmap to embryo implantation: clues from mouse models, Nat. Rev. Genet. 7 (2006) 185–199, https://doi.org/10.1038/nrg1808.

[10] J.-L. Maître, H. Turlier, R. Illukkumbura, B. Eismann, R. Niwayama, F. Nédélec, T. Hiiragi, Asymmetric division of contractile domains couples cell positioning and fate specification, Nat 536 (2016) 344–348, https://doi.org/10.1038/nature18958.

[11] C.J. Chan, M. Costanzo, T. Ruiz-Herrero, G. Monke, R.J. Petrie, M. Bergert, A. Diz-Munoz, L. Mahadevan, T. Hiiragi, Hydraulic control of mammalian embryo size and cell fate, Nat 571 (2019) 112–116, https://doi.org/10.1038/s41586-019-1309-x.

[12] H. Wang, F. Pilla, S. Anderson, S. Martinez-Escribano, I. Herrer, J.M. Moreno-Moya, S. Musti, S. Bocca, S. Oehninger, J.A. Horcajadas, A novel model of human implantation: 3D endometrium-like culture system to study attachment of human trophoblast (Jar) cell spheroids, Mol. Hum. Reprod. 18 (2012) 33–43, https://doi.org/10.1093/molehr/gar064.

[13] Y. You, P. Stelzl, Y. Zhang, J. Porter, H. Liu, A.H. Liao, P.B. Aldo, G. Mor, Novel 3D in vitro models to evaluate trophoblast migration and invasion, Am. J. Reprod. Immunol. 81 (2019), e13076, https://doi.org/10.1111/aji.13076.

[14] N.C. Rivron, J. Frias-Aldeguer, E.J. Vrij, J.C. Boisset, J. Korving, J. Vivie, R. K. Truckenmuller, A. van Oudenaarden, C.A. van Blitterswijk, N. Geijsen, Blastocyst-like structures generated solely from stem cells, Nat 557 (2018) 106, https://doi.org/10.1038/s41586-018-0051-0.

[15] P.T. Ruane, T. Garner, L. Parsons, P.A. Babbington, I. Wangsaputra, S.J. Kimber, A. Stevens, M. Westwood, D.R. Brison, J.D. Aplin, Trophectoderm differentiation to invasive syncytiotrophoblast is promoted by endometrial epithelial cells during human embryo implantation, Hum. Reprod. 37 (2022) 777–792, https://doi.org/10.1093/humrep/deac008.

[16] J.Y. Park, S. Mani, G. Clair, H.M. Olson, V.L. Paurus, C.K. Ansong, C. Blundell, R. Young, J. Kanter, S. Gordon, et al., A microphysiological model of human trophoblast invasion during implantation, Nat. Commun. 13 (2022) 1252, https://doi.org/10.1038/s41467-022-28663-4.

[17] Y. Pu, J. Gingrich, A. Veiga-Lopez, A 3-dimensional microfluidic platform for modeling human extravillous trophoblast invasion and toxicological screening, Lab Chip 21 (2021) 546–557, https://doi.org/10.1039/D0LC01013H.

[18] J. Evans, K.J. Walker, M. Bilandzic, S. Kinnear, L.A. Salamonsen, A novel "embryo-endometrial" adhesion model can potentially predict "receptive" or "non-receptive" endometrium, J. Assist. Reprod. Genet. 37 (2020) 5–16, https://doi.org/10.1007/s10815-019-01629-0.

[19] B. Sozen, A.L. Cox, J. De Jonghe, M. Bao, F. Hollfelder, D.M. Glover, M. Zernicka-Goetz, Self-Organization of mouse stem cells into an extended potential blastoid, Dev. Cell 51 (2019) 698–712 e698, https://doi.org/10.1016/j.devcel.2019.11.014.

[20] J.A. Brassard, M.P. Lutolf, Engineering stem cell self-organization to build better organoids, Cell Stem Cell 24 (2019) 860–876, https://doi.org/10.1016/j.stem.2019.05.005.

[21] A.A. Anlaş, C.M. Nelson, Tissue mechanics regulates form, function, and dysfunction, Curr. Opin. Cell Biol. 54 (2018) 98–105, https://doi.org/10.1016/j.ceb.2018.05.012.

[22] R. Li, C. Zhong, Y. Yu, H. Liu, M. Sakurai, L. Yu, Z. Min, L. Shi, Y. Wei, Y. Takahashi, et al., Generation of blastocyst-like structures from mouse embryonic and adult cell cultures, Cell 179 (2019) 687–702.e618, https://doi.org/10.1016/j.cell.2019.09.029.

[23] H.I.C. Harn, Y.-K. Wang, C.-K. Hsu, Y.-T. Ho, Y.-W. Huang, W.-T. Chiu, H.-H. Lin, C.-M. Cheng, M.-J. Tang, Mechanical coupling of cytoskeletal elasticity and force generation is crucial for understanding the migrating nature of keloid fibroblasts, Exp. Dermatol. 24 (2015) 579–584, https://doi.org/10.1111/exd.12731.

[24] B. Zhang, Q. Luo, X. Mao, B. Xu, L. Yang, Y. Ju, G. Song, A synthetic mechano-growth factor E peptide promotes rat tenocyte migration by lessening cell stiffness and increasing F-actin formation via the FAK-ERK1/2 signaling pathway, Exp. Cell Res. 322 (2014) 208–216, https://doi.org/10.1016/j.yexcr.2014.01.005.

[25] Q. Luo, D. Kuang, B. Zhang, G. Song, Cell stiffness determined by atomic force microscopy and its correlation with cell motility, Biochim. Biophys. Acta Gen. Subj. 1860 (2016) 1953–1960, https://doi.org/10.1016/j.bbagen.2016.06.010.

[26] S. Sart, S.N. Agathos, Y. Li, Engineering stem cell fate with biochemical and biomechanical properties of microcarriers, Biotechnol. Prog. 29 (2013) 1354–1366, https://doi.org/10.1002/btpr.1825.

[27] J. Wang, M. Zou, L. Sun, Y. Cheng, L. Shang, F. Fu, Y. Zhao, Microfluidic generation of Buddha beads-like microcarriers for cell culture, Sci. China Mater. 60 (2017) 857–865, https://doi.org/10.1007/s40843-017-9081-5.

[28] Q.A. Rafiq, K. Coopman, A.W. Nienow, C.J. Hewitt, Systematic microcarrier screening and agitated culture conditions improves human mesenchymal stem cell yield in bioreactors, Biotechnol. J. 11 (2016) 473–486, https://doi.org/10.1002/biot.201400862.

[29] S. Ding, X. Zhao, W. Xiong, L. Ji, M. Jia, Y. Liu, H. Guo, F. Qu, W. Cui, Q. Gu, M. Zhang, Cartilage lacuna-inspired microcarriers drive hyaline neocartilage regeneration, Adv. Mater. (2023), https://doi.org/10.1002/adma.202212114 n/a) 2212114.

[30] S. Ding, X. Liu, X. Zhao, K. Wang, W. Xiong, Z. Gao, C. Sun, M. Jia, C. Li, Q. Gu, M. Zhang, Microcarriers in application for cartilage tissue engineering: recent progress and challenges, Bioact. Mater. 17 (2022) 81–108, https://doi.org/10.1016/j.bioactmat.2022.01.033.

[31] K.Y. Lee, D.J. Mooney, Alginate: properties and biomedical applications, Prog. Polym. Sci. 37 (2012) 106–126, https://doi.org/10.1016/j.progpolymsci.2011.06.003.

[32] O. Chaudhuri, L. Gu, D. Klumpers, M. Darnell, S.A. Bencherif, J.C. Weaver, N. Huebsch, H.P. Lee, E. Lippens, G.N. Duda, D.J. Mooney, Hydrogels with tunable stress relaxation regulate stem cell fate and activity, Nat. Mater. 15 (2016) 326–334, https://doi.org/10.1038/nmat4489.

[33] L. Shang, Y. Cheng, Y. Zhao, Emerging droplet microfluidics, Chem. Rev. 117 (2017) 7964–8040, https://doi.org/10.1021/acs.chemrev.6b00848.

[34] S. Utech, R. Prodanovic, A.S. Mao, R. Ostafe, D.J. Mooney, D.A. Weitz, Microfluidic generation of monodisperse, structurally homogeneous alginate microgels for cell encapsulation and 3D cell culture, Adv. Healthc. Mater. 4 (2015) 1628–1633, https://doi.org/10.1002/adhm.201500021.

[35] M. Giakoumopoulos, T.G. Golos, Embryonic stem cell-derived trophoblast differentiation: a comparative review of the biology, function, and signaling mechanisms, J. Endocrinol. 216 (2013) R33–R45, https://doi.org/10.1530/JOE-12-0433.

[36] Z. Gu, J. Guo, J. Zhai, G. Feng, X. Wang, Z. Gao, K. Li, S. Ji, L. Wang, Y.J.A.S. Xu, A uterus-inspired niche drives blastocyst development to the early organogenesis, Adv. Sci. 2202282 (2022), https://doi.org/10.1002/advs.202202282.

[37] C.R. Jones-Paris, S. Paria, T. Berg, J. Saus, G. Bhave, B.C. Paria, B.G. Hudson, Embryo implantation triggers dynamic spatiotemporal expression of the basement membrane toolkit during uterine reprogramming, Matrix Biol. 57–58 (2017) 347–365, https://doi.org/10.1016/j.matbio.2016.09.005.

[38] B.C. Paria, J. Reese, S.K. Das, S.K. Dey, Deciphering the cross-talk of implantation: advances and challenges, Science 296 (2002) 2185–2188, https://doi.org/10.1126/science.1071601.

[39] C.E. Brinckerhoff, L.M. Matrisian, Matrix metalloproteinases: a tail of a frog that became a prince, Nat. Rev. Mol. Cell Biol. (3) (2002) 207–214, https://doi.org/10.1038/nrm763.

[40] M. Amano, M. Nakayama, K. Kaibuchi, Rho-kinase/ROCK: a key regulator of the cytoskeleton and cell polarity, Cytoskeleton 67 (2010) 545–554, https://doi.org/10.1002/cm.20472.

[41] H.-B. Wang, M. Dembo, K. Hanks Steven, Y.-l. Wang, Focal adhesion kinase is involved in mechanosensing during fibroblast migration, Proc. Natl. Acad. Sci. USA 98 (2001) 11295–11300, https://doi.org/10.1073/pnas.201201198.

[42] S. SenGupta, C.A. Parent, J.E. Bear, The principles of directed cell migration, Nat. Rev. Mol. Cell Biol. 22 (2021) 529–547, https://doi.org/10.1038/s41580-021-00366-6.

[43] J. Park, D.-H. Kim, H.-N. Kim, C.J. Wang, M.K. Kwak, E. Hur, K.-Y. Suh, S.S. An, A. Levchenko, Directed migration of cancer cells guided by the graded texture of the underlying matrix, Nat. Mater. 15 (2016) 792–801, https://doi.org/10.1038/nmat4586.

[44] B.-K. Lee, Y.j. Jang, M. Kim, L. LeBlanc, C. Rhee, J. Lee, S. Beck, W. Shen, J. Kim, Super-enhancer-guided mapping of regulatory networks controlling mouse trophoblast stem cells, Nat. Commun. 10 (2019), https://doi.org/10.1038/s41467-019-12720-6.

[45] D. Kiyozumi, I. Nakano, R. Sato-Nishiuchi, S. Tanaka, K. Sekiguchi, Laminin is the ECM niche for trophoblast stem cells, Life Sci. Alliance 3 (2020), https://doi.org/10.26508/lsa.201900515.

[46] J.A. Eble, S. Niland, The extracellular matrix in tumor progression and metastasis, Clin. Exp. Metastasis 36 (2019) 171–198, https://doi.org/10.1007/s10585-019-09966-1.

[47] S. Patwardhan, P. Mahadik, O. Shetty, S. Sen, ECM stiffness-tuned exosomes drive breast cancer motility through thrombospondin-1, Biomaterials 279 (2021), 121185, https://doi.org/10.1016/j.biomaterials.2021.121185.

[48] J.L. Leight, A.P. Drain, V.M. Weaver, Extracellular matrix remodeling and stiffening modulate tumor phenotype and treatment response, Annu. Rev. Cell Biol. 1 (2017) 313–334, https://doi.org/10.1146/annurev-cancerbio-050216-034431.

[49] K. Hayakawa, E. Himeno, S. Tanaka, T. Kunath, Isolation and manipulation of mouse trophoblast stem cells, Curr. Protoc. Stem. Cell. Biol. 32 (2015), https://doi.org/10.1002/9780470151808.sc01e04s32, 1E.4.1-1E.4.32.

[50] S. Tanaka, T. Kunath, A.-K. Hadjantonakis, A. Nagy, J. Rossant, Promotion of trophoblast stem cell proliferation by FGF4, Science 282 (1998) 2072–2075, https://doi.org/10.1126/science.282.5396.2072.

[51] T. Strunz, K. Oroszlan, R. Schäfer, H.-J. Güntherodt, Dynamic force spectroscopy of single DNA molecules, Proc. Natl. Acad. Sci. USA 96 (1999), 11277, https://doi.org/10.1073/pnas.96.20.11277.

[52] Z. Zhong, S. Liang, E. Sanchez-Lopez, F. He, S. Shalapour, X.-j. Lin, J. Wong, S. Ding, E. Seki, B. Schnabl, et al., New mitochondrial DNA synthesis enables NLRP3 inflammasome activation, Nat 560 (2018) 198–203, https://doi.org/10.1038/s41586-018-0372-z.

[53] Y. Liao, G.K. Smyth, W. Shi, featureCounts: an efficient general purpose program for assigning sequence reads to genomic features, Bioinformatics 30 (2014) 923–930, https://doi.org/10.1093/bioinformatics/btt656.

[54] M.I. Love, W. Huber, S. Anders, Moderated estimation of fold change and dispersion for RNA-seq data with DESeq2, Genome Biol. 15 (2014) 550, https://doi.org/10.1186/s13059-014-0550-8.

[55] T. Wu, E. Hu, S. Xu, M. Chen, P. Guo, Z. Dai, T. Feng, L. Zhou, W. Tang, L. Zhan, et al., clusterProfiler 4.0: a universal enrichment tool for interpreting omics data, Innovations 2 (2021), https://doi.org/10.1016/j.xinn.2021.100141.